ADVANCED MATERIALS INTERFACES
www.advmatinterfaces.de

Atomic Level 1D Structural Modulations at the Negatively Charged Domain Walls in $BiFeO_3$ Films

Wen-Yuan Wang, Yun-Long Tang, Yin-Lian Zhu, Yao-Bin Xu, Ying Liu, Yu-Jia Wang, Suriyaprakash Jagadeesh, and Xiu-Liang Ma**

Charged domain walls (CDWs) show great potentials to mediate the properties of ferroelectrics. Direct mapping of these domain walls at an atomic scale is of critical importance for understanding the domain wall dominated properties. Here, based on aberration-corrected scanning transmission electron microscopy, tail-to-tail CDWs at 71°, 109°, and 180° domains in $BiFeO_3$ thin films have been identified. 2D mappings demonstrate 1D structural modulations with alternate lattice expansions and clockwise/counterclockwise lattice rotations at these CDWs. Such behaviors of CDWs reveal a remarkable contrast to the uncharged domain walls and imply delicate interactions between bound charges and structural compensations of domain wall. These results are expected to provide new information on domain wall structures and shed some light on the understanding of domain wall properties in ferroelectrics.

1. Introduction

Domain walls (DWs) in perovskite ferroelectrics are special interfaces that separate domains with electric dipoles aligned in different directions.[1,2] Different from domain matrix, they are known to exhibit various intriguing properties which have great potentials in information storage, sensors, and photoelectric devices, especially as the size of electric devices is shrinking.[3–10] Technically, the geometries of DWs can be manipulated by external electric field and as-grown boundary conditions, and consequently they are able to be patterned into related electrical elements.[11,12] In addition, the functionalities of DWs actually can be modulated by appropriately controlling DW orientation-related charging characters, which is expected to open a broad diagram of potential property designation.[13,14]

Depending on the orientations of DWs, the dipole configurations beside DWs can either be "head-to-tail," "head-to-head" or "tail-to-tail" which then introduce zero, net positive or net negative bound charges at the DWs, respectively. Nearly 40 years ago, Vul et al. proposed that charged DWs (CDWs, adopt "head-to-head" or "tail-to-tail" dipole arrangements) would accumulate huge number of free charge carriers that can result in a metallic conductance at the DWs in insulating ferroelectrics.[15] Such a CDW-induced enhancement of domain wall conductivity has been convinced recently in $BaTiO_3$,[5] $LiNbO_3$,[16] improper ferroelectric $ErMnO_3$,[13] and $HoMnO_3$.[17] Nevertheless, atomic structures of CDWs which are greatly important for understanding the novel DW phenomenon are still inadequate, although aberration-corrected transmission electron microscopy has been applied to several CDWs in tetragonal $PbTiO_3$,[18] $PbZr_{0.2}Ti_{0.8}O_3$,[19] hexagonal $YMnO_3$.[20] The 90° and 180° CDWs in $PbTiO_3$ and $PbZr_{0.2}Ti_{0.8}O_3$ are in a broadened fashion where the electric dipoles are smaller than the bulk value;[18,19] reduction of Mn–O distances at CDW were revealed in $YMnO_3$.[20] All these CDWs exhibit novel characters remarkably distinct from the uncharged ones.

Rhombohedral multiferroic $BiFeO_3$ (BFO) possesses various kinds of DWs which feature 109°, 180°, and 71° configurations, respectively. Since the finding of novel DW conduction in BFO, several emergent phenomena at DWs are confirmed, such as electrically tunable conductance, enhanced photovoltage and magnetoresistant effect.[8,14,21] Particularly, CDWs in BFO exhibit electrically controlled photodetection property which implies nonvolatile optoelectronic memory applications.[21] In addition, these CDWs are also known to exhibit pinning effects on the movement of DWs and thus induce polarization fatigue in BFO memories. Although a charge-accumulation driven T phase was identified at a 71° CDW with "head-to-head" polarizations,[22] atomic-scale mapping of tail-to-tail CDWs in BFO films is still so incomprehensive that the physical insights of the CDW phenomena are known little.

Here, using aberration-corrected scanning transmission electron microscopy (STEM), negatively CDWs in BFO films were systematically investigated, with their structures being directly mapped on the atomic scale. 109°, 180°, and 71° CDWs on (100) plane and a 109° CDW on (110) plane, with tail-to-tail dipole configurations, are thus revealed. Unusual 1D structural modulations characterized by alternate lattice expansions and clockwise/counterclockwise lattice rotations along the corresponding DWs are found, which differ remarkably from both uncharged domain walls (UCDWs) and positively CDW with head-to-head polarizations in BFO reported previously.[3,22–25] These findings are expected to broaden our understanding on DW structures as well as the effect of bound charges on structural stabilities of

W.-Y. Wang, Dr. Y.-L. Tang, Prof. Y.-L. Zhu, Y.-B. Xu, Y. Liu, Dr. Y.-J. Wang, S. Jagadeesh, Prof. X.-L. Ma
Shenyang National Laboratory for Materials Science
Institute of Metal Research
Chinese Academy of Sciences
Wenhua Road 72, 110016 Shenyang, China
E-mail: ylzhu@imr.ac.cn; xlma@imr.ac.cn

DOI: 10.1002/admi.201500024

 © 2015 WILEY-VCH Verlag GmbH & Co. KGaA, Weinheim

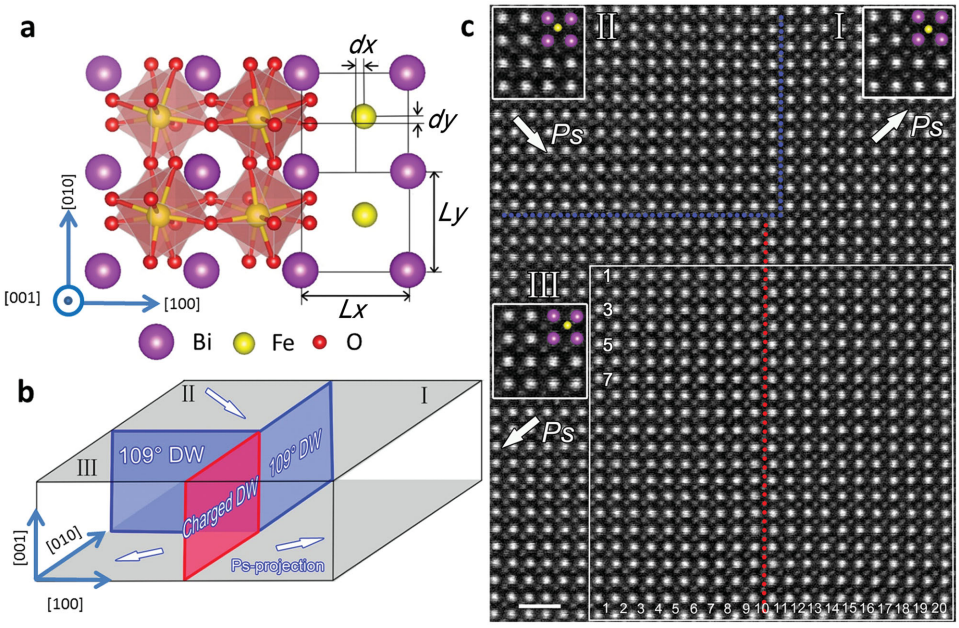

Figure 1. Illustration of 109° CDW of (100) type. a) Atomic model of multiferroic BFO projected along [001] direction where Bi, Fe, and O are represented by violet, yellow, and red spheres, respectively. *dx* and *dy* are components of sublattice displacement vectors of Fe sublattice D_F (from Bi sublattice center to Fe sublattice) in horizontal and vertical directions. *Lx* and *Ly* are the lattice spacing in horizontal and vertical directions. b) Illustration of intersection of three domains I, II, and III, the white arrows are the *Ps* projections of the corresponding domains along [001] direction. The blue planes are 109° UCDWs of (100) type. The red plane is 109° CDW of (100) type. c) A HAADF image of domain intersection projected along [001]. The 109° UCDWs of (100) type is marked by blue dotted lines. A red dotted line indicates the 109° CDW of (100) type. The insets are the enlarged images of the corresponding area (violet: Bi, yellow: Fe). The white arrows are the *Ps* projections. The square frame is the area used for analyzing the lattice variations and Fe sublattice displacements. Scale bar: 1 nm.

DWs. This study may also provide atomic-scale information to the theoretical studies on CDW related phenomena.

2. Results and Discussion

2.1. General Information

BFO thin films were epitaxially grown on $SrTiO_3$(STO) (001) and $GdScO_3$(GSO) $(110)_{orthorhombic}$ single-crystal substrates by pulsed laser deposition (PLD). The choice of the STO substrate is to introduce CDW by making use of the fourfold symmetry of the cubic structure in STO.[26] The BFO films grown on GSO are further buffered with an epitaxial and conducting $SrRuO_3$(SRO) layer which will promote introduction of 71° CDW through surface-compensating.[22,27] The bulk BFO with Curie temperature ≈1103 K and Neel temperature ≈640 K has a distorted perovskite structure (space group *R*3*c*) where Bi atom sits at corner, Fe atom shifts from the body center of pseudocubic structure along ⟨111⟩ axes as well as O atoms which comprise a distorted octahedron[28] (**Figure 1**a). The relative atomic displacement can be used to evaluate the polarization (ordered parameter) of perovskite ferroelectrics,[18,19,22,23,29–32] for it results in the center of positive and negative charge separating from each other and causes an electrical dipole pointing from negative charge center to positive charge center. In pseudocubic ⟨100⟩ directions, the spontaneous polarization vector projection (*Ps* projection) can be represented by $-D_F$ pointing from Fe to the mass center of Bi sublattice (*–dx* and *–dy* in Figure 1a). To visualize these structural changes, lattice spacing [specifically, horizontal lattice (*Lx*) and vertical lattice (*Ly*)] in Figure 1a and lattice rotations [horizontal lattice rotation (*Rx*) and vertical lattice rotation (*Ry*)] in **Figure 2**b are introduced.

In rhombohedral BFO, there are four ferroelastic variants (r_1–r_4) while each of these ferroelastic variants has two ferroelectric variants along ⟨111⟩[28] (Figure S1a, Supporting Information). The polarization direction of two adjacent domains could then be 109°, 180° or 71°, and the corresponding uncharged domain walls have certain geometries: 109° UCDW on {100} plane, 180° UCDW on {110} plane, and 71° UCDW on {110} plane (Figure S1a–e, Supporting Information).[12,23,33] Using these UCDWs as references, CDWs with tail-to-tail dipole configuration in BFO can be identified. (More details about determination of CDW types are in the Supporting Information.)

2.2. 109° CDWs of (100) Type

Figure 1b is a schematic showing the configurations of domain walls. There are three ferroelectric variants named I, II, and III, respectively. From the *Ps* projections given here (white arrows), two 109° UCDWs on (100) and (010) planes noted by blue shaded areas (defined as 109° UCDWs of (100) type), and a 109° CDW on (100) plane noted by red shaded area (defined as 109° CDWs of (100) type) are determined. Figure 1c displays an atomic resolved high angle annular dark field (HAADF) image of the corresponding domain pattern taken along [001]

© 2015 WILEY-VCH Verlag GmbH & Co. KGaA, Weinheim

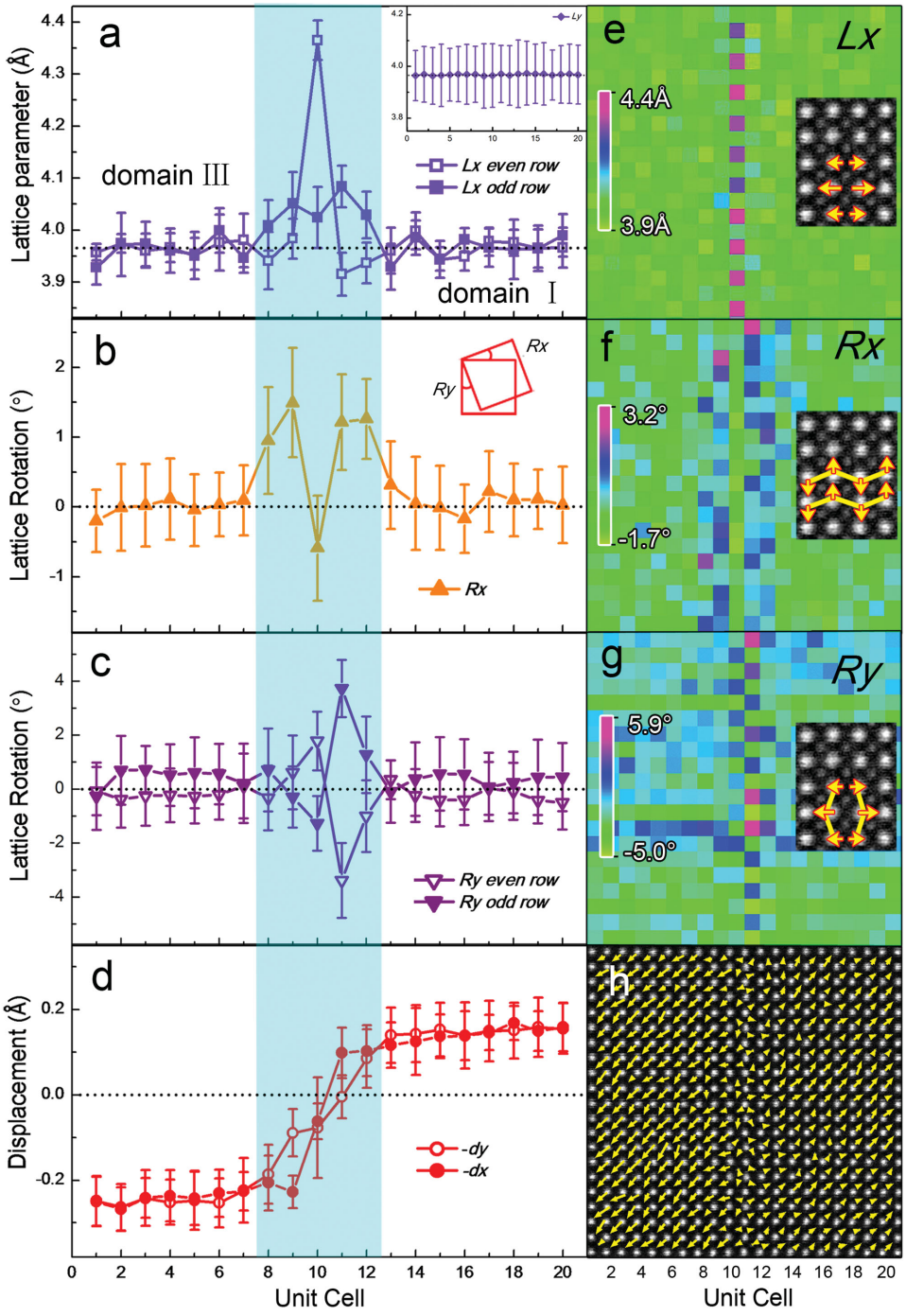

Figure 2. Quantitative analysis of 109° CDW of (100) type. a–d) Line profiles of lattice spacing *Lx* (inset is *Ly*), horizontal lattice rotation *Rx*, vertical lattice rotation *Ry* (odd row rotation, even row rotation), and $-dx$ and $-dy$ across 109° CDW of (100) type. The positive rotation value denotes an anti-clockwise rotation and negative value denotes a clockwise rotation. The blue area denotes the domain wall width. e–h) Unit-cell-wise 2D mappings of *Lx*, *Rx*, *Ry*, and $-D_F$. The insets are the enlarged area of the CDW showing exaggeratedly how these lattices change.

zone axis. The *Ps* projections of domain I, II III can easily be identified by noting $-D_F$ in three magnified insets overlaying the corresponding domains, where violet circles denote Bi columns and yellow circles denote Fe columns. Two blue dashed lines denote the 109° UCDWs of (100) type with "head-to-tail" *Ps* projections along different diagonal directions. The red dashed line denotes the existence of 109° CDW of (100) type with "tail-to-tail" *Ps* projections.

Figure 2a–h shows statistical line profiles and unit-cell-wise 2D mappings of these structural variations across the 109° CDW of (100) type. For the horizontal lattice spacing, unique 1D structural modulation emerges: the *Lx* shows

© 2015 WILEY-VCH Verlag GmbH & Co. KGaA, Weinheim

obvious alternate expansion along the CDW (Figure 2a). The *Lx* in even rows exhibits an abrupt increase within one unit cell at the CDW while *Lx* in odd rows increases slowly in a range of about five unit cells laterally across the CDW. The lattice expansions in the even rows are as high as ≈10% (4.36 Å) compared with the typical domain lattice spacing of 3.965 Å. Furthermore, in Figure 2e the 2D mapping obviously displays the different magnitude of *Lx* expansion in odd and even rows (depicted by the yellow arrow in the inset), which also reveals the 1D structural modulation of *Lx* along the CDW. Such modulation is constrained within the width of CDW and has a period of two unit cells. For *Ly*, however, no modulation is detected and a constant value is maintained, as shown in the inset of Figure 2a and 2D mapping in Figure S3a, Supporting Information.

The structural features of 109° CDW can also be identified from the lattice rotations in horizontal and vertical directions. The definitions of horizontal and vertical lattice rotation (*Rx* and *Ry*) are shown as inset in Figure 2b. Actually, the lattice rotations are a kind of lattice strain. The *Rx* away from the CDW is uniform and normalized to zero as a reference. Near the CDW, the *Rx* shows two sharp peaks symmetrically distributed beside the CDW, where the positive value represents anticlockwise lattice rotation. In the CDW center, however, the unit cell rotates in clockwise with a small negative value. Such symmetrical distribution of *Rx* near the CDW maintains along the whole CDW according to the 2D mapping shown in Figure 2f (depicted by yellow arrows and zigzag sticks in the inset). Figure 2c shows the fluctuation of *Ry* values at two sides of CDW. It is noted that two curves can be drawn from odd and even rows, respectively. From the left to right, the values keep nearly constant; when approaching the CDW, the points from odd rows go down for about three unit cells then go up sharply for one unit cell and down again. The points from even rows behave conversely: initially go up, then down and up again. This rotation difference in odd rows and even rows actually generates a 1D structural modulation with a period of two unit cells along the CDW, which is similar to the modulation of lattice spacing *Lx* (Figure 2g, depicted by yellow arrows and zigzag sticks in the inset). In fact, the modulations in lattice spacing and lattice rotation are in line with each other, as the lattice spacing expansion must result in the corresponding changes in lattice rotation, i.e., the different expansion of *Lx* (Figure 2e) will unambiguously induce alternate clockwise/counterclockwise *Ry* (Figure 2g) across the CDW, which unequivocally forms a unique 1D modulations along the CDW.

The Fe sublattice displacement vectors across the 109° CDW of (100) type are shown in Figure 2d (*–dx*, *–dy*). It is obvious that apart from the CDW (about five unit cells), the displacements are almost invariable which are consistent with the bulk value,[23] while at the CDW, the displacements symmetrically decrease from bulk value to nearly zero, and are further visualized in the 2D mapping shown in Figure 2h.

The structures of 109° CDW and UCDW of (100) type are rather different. According to previous theoretical calculations and experiments[24,25] as well as our experimental results (Figure S2, Supporting Information), only the horizontal lattice rotation *Rx* of the 109° UCDW of (100) type has noticeable changes at the DW while all other variations such as *Lx*, *Ly*, and *Ry* basically maintain the same value of bulk BFO. Such difference in structure variation between 109° UCDW and CDW of (100) type would be related to the different configurations of electrical dipoles beside the DW. The unique "tail-to-tail" dipole arrangement of the 109° CDW of (100) type triggers accumulation of bound charges, which result in elevation of electrostatic energy. Local structural modification might be helpful to reduce the electrostatic energy of the CDWs.[18,19,22]

2.3. 109° CDW of (110) Type

Figure 3a is an illustration of the intersection of three domain walls: namely 109° CDW of (110) type (red plane) and two 109° UCDWs of (100) type (blue planes). The corresponding ferroelectric variants (I, II, III) and their *Ps* projections along [001] direction are depicted. Figure 3b is an atomic resolved HAADF image of the corresponding 109° CDW of (110) type in [001] zone axis. The location of domain wall is depicted by a red dotted line. The structural parameters shown in Figure 3f–h are extracted from the region with white parallelogram frame. The horizontal lattice spacing (*Lx*) features an increase over four unit cells transversely the CDW (seen in Figure 3f). Such expansion of *Lx* is unvaryingly distributed along CDW, which can be visualized directly by 2D mapping in Figure 3c. Similar feature is also obtained for the vertical lattice spacing (*Ly*) showed by inset in Figure 3f and by 2D mapping in Figure S3d, Supporting Information. The calculated lattice rotations are plotted against the unit cell positions and displayed in Figure 3g. The values of horizontal lattice rotation (*Rx)* and vertical lattice rotation (*Ry)* are opposite to each other, ranging four unit cells at CDW. And the 2D mappings of *Rx* and *Ry* verify the homogeneous distribution of the lattice rotation at CDW seen in Figure 3d and Figure S3e, Supporting Information. For the Fe sublattice displacement in Figure 3h, *–dx* and *–dy* are gradually decreasing to zero and then return to the bulk value across the CDW.

It is obvious that the lattice spacing and rotation of the 109° CDW of (110) type are distinct from those of the (100) type as discussed above. Interestingly, the one-directional structural modulation at 109° CDW of (100) type disappears in (110) type domain wall. Instead, it acquires a uniform distribution of lattice distortion. Such difference in structures between 109° CDWs of (100) type and (110) type imply that, the influence of bound charge on the structures of CDWs is moderately complex. In fact, the particulars of the bound charge should include the nature (positive or negative) and the amount. Our previous work explicated the different structural features at positively and negatively CDWs in PTO,[18] which helps to acquaint about the nature of the charges. Furthermore, the amounts of bound charges, which depend only on the component of *Ps* normal to the DWs,[13] are totally different for 109° CDWs of (100) and (110) type, and would be a reason for different structures of 109° CDWs of (100) and (110) type. Further insight about this point would be inferred based on structural compensations at 180° and 71° CDWs of (100) type discussed below.

© 2015 WILEY-VCH Verlag GmbH & Co. KGaA, Weinheim

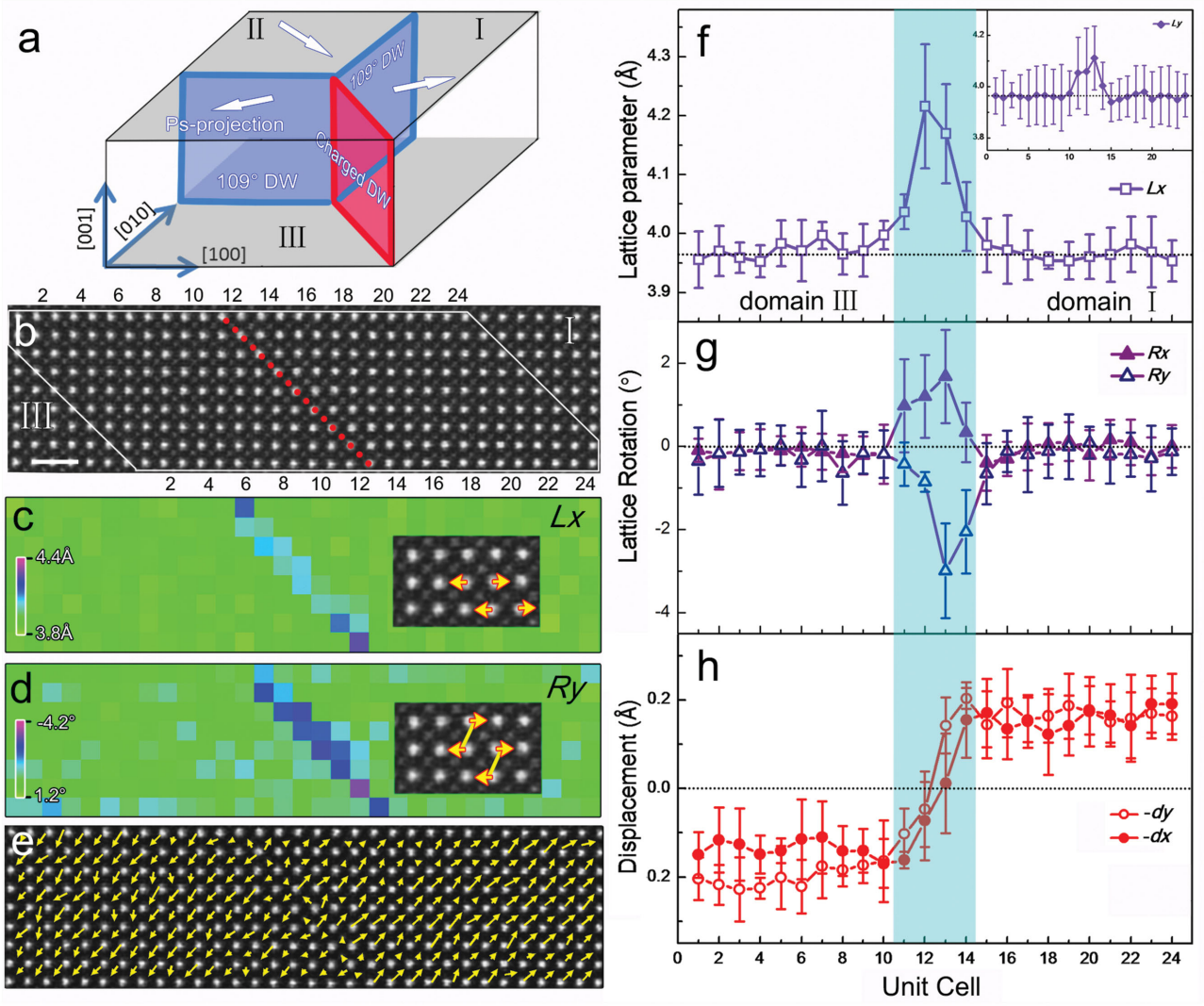

Figure 3. Illustration of 109° CDW of (110) type and quantitative analysis. a) Illustration of intersection of three domains I, II, and III. The white arrows are the corresponding *Ps* projections along [001] direction. The blue planes are 109° UCDWs of (100) type. The red plane is 109° CDW of (110) type. b) A HAADF image of the 109° CDW of (110) type in [001] zone axis. The red dotted line denotes the domain wall. The area surrounded by white parallelogram is used to quantitative analyze. The number represents unit cells in same column parallel to the domain wall. Scale bar: 1 nm. c–e) Unit cell wise 2D mappings of *Lx*, *Ry*, and $-D_F$. The insets are the enlarged areas of the CDW showing exaggeratedly how these lattices change. f–h) Line profiles of *Lx* (inset is *Ly*), *Rx* and *Ry*, *–dx* and *–dy* across the 109° CDW of (110) type. The blue area denotes the domain wall width.

2.4. 180° CDWs of (100) Type

In **Figure 4**a a schematic of 180° CDW of (100) type of red plane intersecting with a blue plane of 180° UCDW of (100) type is depicted. There are two ferroelectric variants IV and V with their *Ps* projections along [001] direction noted by arrows. Figure 4b shows an atomic resolved HAADF image of the 180° CDW of (100) type in [001] zone axis. The domain wall is labeled by a red dotted line. Figure 4c displays the behaviors of lattice spacing across the CDW where the *Lx* can be divided into two kinds: odd rows and even rows. The *Lx* in odd rows expands abruptly and shows a sharp peak within one unit cell, while the *Lx* in even rows expands pretty slighter and extends to three unit cells. In contrast, the lattice spacing *Ly* is unchanged across the CDW (inset in Figure 4c). The 2D mapping of the *Lx* is shown in **Figure 5**a. 1D lattice modulation can be clearly noticed which is similar to the 109° CDW of (100) type. For the lattice rotation, the *Rx* in Figure 4d shows two positive peaks in the CDW, the distribution of which, along the CDW is uniform and clearly seen in Figure 5b. The *Ry* revealed in Figure 4e, which obtains opposite rotation for lattice in odd and even rows, both of which showing alternate rotation (positive value/negative value) at the area of CDW. Such kind of behavior is clearly demonstrated in the 2D mapping of *Ry* in Figure 5c. The Fe sublattice displacement across the CDW shown in Figure 4f (*–dx*, *–dy*) and Figure 5d ($-D_F$) exhibits similar features as the 109° CDW of (100) type and (110) type.

© 2015 WILEY-VCH Verlag GmbH & Co. KGaA, Weinheim

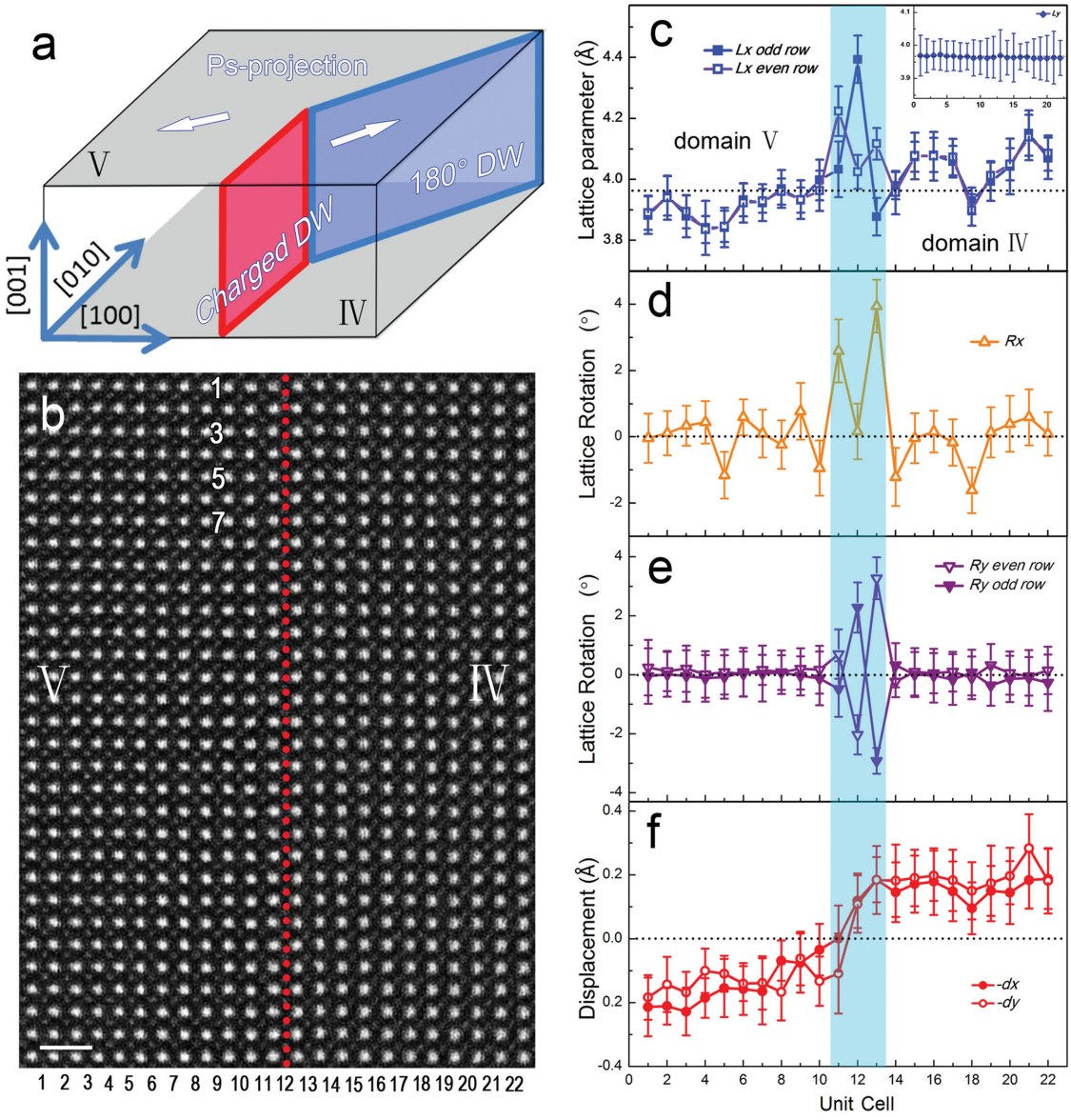

Figure 4. Illustration of 180° CDW of (100) type and quantitative analysis. a) Illustration of intersection of two domains IV and V, where the blue plane represents 180° UCDW of (110) type and the red plane represents 180° CDW of (100) type. The white arrows are the *Ps* projections. b) A HAADF image of the 180° CDW of (100) type in [001] zone axis. The red dotted line denotes the domain wall. Scale bar: 1 nm. c–f) Line profiles of *Lx* (inset is *Ly*), *Rx*, *Ry* (odd row rotation and even row rotation), *–dx* and *–dy* across 180° CDW of (100) type. The blue area denotes the domain wall width.

2.5. 71° CDW of (100) Type

Figure 6a depicts a 71° CDW of (100) type with red plane, which are comprised by three ferroelectric variants VI, VII, and VIII. Three arrows depict the *Ps* projections of the corresponding domains along [001] direction. A 180° UCDW of (110) type and a 109° UCDW of (100) type are denoted by two blue planes. An atomic resolved HAADF image of 71° CDW of (100) type in [001] zone axis is displayed in Figure 6b and exploited for quantitative investigation. The location of domain wall is depicted by a red dotted line. We encountered the same phenomenon of the lattice spacing *Lx* and *Ly* variation across the CDW, which is similar to the 109° and 180° CDW of (100) type. The *Lx* in odd rows shows a sharp peak whereas the *Lx* in even rows shows a relatively small increase with a wide range across the CDW, which indicates obvious 1D structural modulation. 2D mapping of the *Lx* in Figure 6c convinces such 1D modulation. The horizontal and vertical lattice rotations across the domain wall are shown in Figure 6h,i, respectively. In Figure 6h the *Rx* shows two opposite peaks of one unit cell besides the center of CDW, shown clearly in Figure 6d. The *Ry* revealed in Figure 6i includes two kinds (odd rows and even rows) and fluctuates in opposite directions over about three unit cells. The fluctuation of *Ry* at the CDW is shown in 2D mapping in Figure 6e. The Fe sublattice displacement is schematically represented in Figure 6f,j.

It is apparent that the structures of (100) type CDWs of 109°, 180°, and 71° show some sort of similarity. All *Lx* show similar

© 2015 WILEY-VCH Verlag GmbH & Co. KGaA, Weinheim

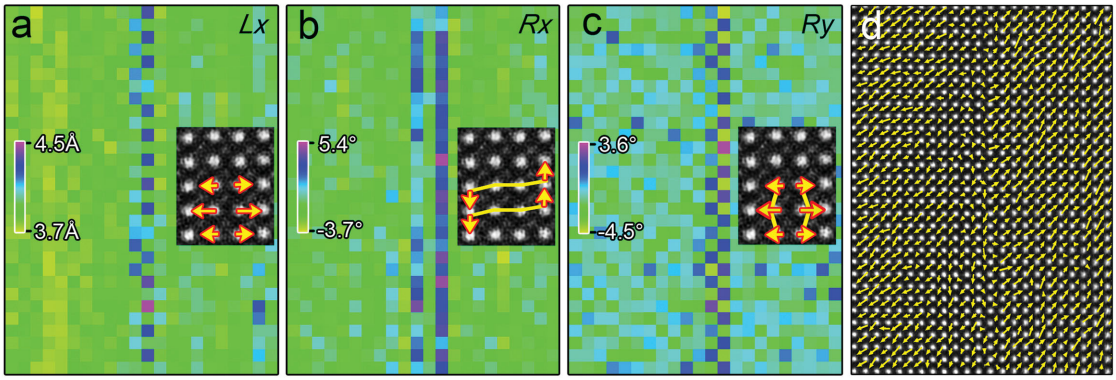

Figure 5. 2D distribution of lattice variation and *Ps* projection of the 180° CDW of (100) type. a–d) Unit cell wise 2D mappings of *Lx*, *Rx*, *Ry*, and $-D_F$. The insets are the enlarged area of the CDW showing directly how these lattices change.

1D modulation: a huge expansion followed by a relatively small expansion along the domain wall, which is observed consecutively, while all *Ly* reside relatively constant. In addition, *Rx* and *Ry* also show similarities: the *Rx* of 109° and 180° CDWs expose two sharp peaks due to the anticlockwise lattice rotations. And alternating anticlockwise/clockwise lattice rotations of *Ry* hold for all the three types of CDWs on (100) plane. In fact, these CDWs of (100) type also possess equal amount of bound charges, since the amount of bound charges is determined by the component of *Ps* normal to the DW. It has been pointed out that these bound charges have critical influence on structural compensation of CDWs.[18,19,22] To a certain degree, it is reasonable to ascribe these similar structural characters of the CDWs to the identical amount of corresponding bound charges. This proposal can be further verified by the fact that 109° CDWs of (100) type and (110) type show absolutely different structural variations, where the amount of bound charges of each CDW are different.

In contrast to novel structural modulations, the impact of bound charges on DW properties has been reported in several ferroelectrics. Meier et al.[13] demonstrated a continuous function of DW conductance versus DW orientations, where the character (positive or negative charges) and the amount of bound charges vary continuously depending on DW orientations. Such orientation controlled bound charges can even mediate the magnitude of CDW conductance on two orders.[14,16] The explanations of above observations, which are in principle based on the model proposed by Vul et al.,[15] are all attributed to the bound charge induced accumulation of free charge carriers.[34,35] Nevertheless, our results imply that the structural variations at CDWs and their orientation dependence should also be taken into account since these structural features would indicate different electron state existing at CDWs.

Our results also demonstrate an atomic scale methodology to identify CDW configurations with the reference of UCDWs in the rhombohedral ferroelectrics. It is worthwhile to mention that all the above HAADF images of negatively CDWs apparently display unusual *Ps* configurations. Such an anomaly results from the fact that the *Ps* vectors seen in the images are actually projected values. For example, the projected *Ps* beside domain I and III in Figure 1c forms a relationship of 109° although it is likely a 180° configuration; situations are still similar for the 109° CDW of (110) type (Figure 3) and 71° CDW of (100) type (Figure 6). Via aid of the UCDWs, such as 109° and 180° UCDWs, the complex details of the negatively CDWs can be uniquely revealed. This method can be extrapolated further for studying complicated DWs in other kinds of rhombohedral ferroelectrics.

The information on domain wall structures is also expected to greatly facilitate the theoretical studies on ferroelectrics. For example, based on the atomic-scale information of domain walls, phase-field modeling indicates that the Bloch and Neel features existing at 180° DW in $BaTiO_3$ are due to the structural distortions of the DW.[36] In other words, the atomic-scale information is of fundamental importance when theoretical calculations (first principle calculation, phase-field modeling, or other calculations) are employed to study the CDWs for better understanding the physical nature and predicting various novel properties of DWs. On the other hand, it is known that the influence of substrate restriction on the DW structures in PTO thin films is demonstrated,[18] in which variant structural features of DW are found in the area close to and away from the film/substrate interface. The effect of strain on the structures of CDWs in BFO is also worthwhile to be explored in the future, although the misfit between BFO and GSO in the present study is as small as 0.13%.

3. Conclusion

The 109°, 180°, and 71° negatively CDWs on (100) plane and a 109° negatively CDW on (110) plane in BFO thin films are identified. Both the atomic structural details and sublattice ferroelectric ion displacements of these CDWs are quantitatively studied using aberration corrected HAADF-STEM with sub-angstrom precision. Lattice spacing *Lx* and lattice rotation *Ry* at the CDWs of (100) type show 1D modulations where alternate lattice expansions and clockwise/anticlockwise rotations are clearly imaged. These findings imply the presence of complex interactions between structural compensations and bound charges of domain wall. The present study will be helpful for understanding DW structures and the role of bound charges on DW structures, which consequently may shed some light on comprehension of the physical nature of DW properties.

© 2015 WILEY-VCH Verlag GmbH & Co. KGaA, Weinheim

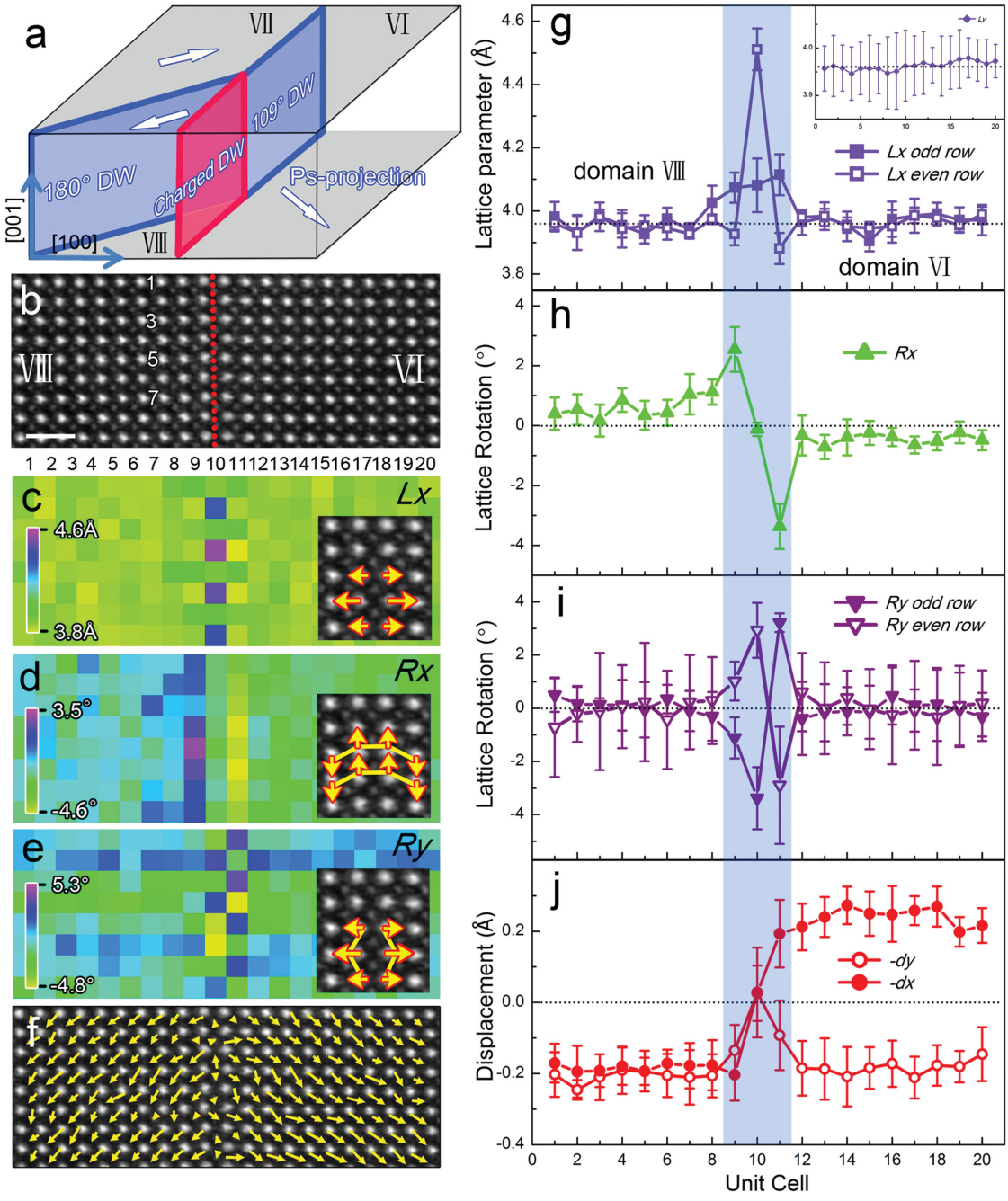

Figure 6. Illustration of 71° CDW of (100) type and quantitative analysis. a) Illustration of intersection of three domains VI, VII, and VIII. The white arrows are the *Ps* projections along [001] direction. The blue planes are 109° UCDW of (100) type and 180° UCDW of (110) type. The red plane is 71° CDW of (110) type. b) A HAADF image of the 71° CDW of (100) type in [001] zone axis. The red dotted line denotes the domain wall. The number represents unit cells in same column parallel to the domain wall. Scale bar: 1 nm. c–f) Unit cell wise 2D mappings of *Lx*, *Rx*, *Ry*, and $-D_F$. The insets are the enlarged areas of the CDW showing exaggeratedly how these lattices change. g–j) Line profiles of *Lx* (inset is *Ly*), *Rx* and *Ry*, $-dx$ and $-dy$ across 71° CDW of (100) type. The blue area denotes the domain wall width.

4. Experimental Section

BFO thin films were epitaxially grown on STO (001) and GSO (110) single-crystal substrates by PLD using a KrF ($\lambda = 248$ nm) excimer laser. During the growth, the substrates temperature were kept at 680 °C, with a oxygen pressure of 13 Pa, a laser repetition of 10 Hz for BFO and 2 Hz for SRO. After deposition, the films were in situ annealed at 680 °C for 30 min in pure O_2 under 5×10^4 Pa. TEM samples were made by slicing, gluing, grinding, and final ion milling with a Gatan PIPS 691. STEM images were recorded using the high-angle angular dark-field detector on FEI Titan G2 60–300 kV microscopy equipped with a high-brightness field-emission gun, double Cs correctors, and a monochromator operating at 300 kV. The probe convergence is 25 mrad which yields a probe size of less than 1 Å. Before quantitative analysis, HAADF-STEM

© 2015 WILEY-VCH Verlag GmbH & Co. KGaA, Weinheim

images were performed by fast Fourier transform (FFT) filtering using only a low-pass annular mask (slightly more than the resolution limit of the image). The atomic position was determined by 2D Gaussian fitting of the individual atomic intensity profile of the STEM image using Matlab.[18,19,22,23,37] 2D mapping of lattice spacing, lattice rotation, and Fe sublattice displacement was also carried out using Matlab and Gatan DigitalMicrography software.

Supporting Information

Supporting Information is available from the Wiley Online Library or from the author.

Acknowledgements

This work was supported by the National Natural Science Foundation of China (Grant Nos. 51231007 and 51171190) and National Basic Research Program of China (Grant Nos. 2014CB921002 and 2009CB623705). W. Y. Wang and Y. L. Tang contributed equally in this work. The authors are grateful to B. Wu and L. X. Yang of this laboratory for their technical supports on the Titan platform of G2 60-300kV aberration-corrected scanning transmission electron microscope.

Received: January 16, 2015
Revised: March 24, 2015
Published online:

[1] M. Dawber, K. M. Rabe, J. F. Scott, *Rev. Mod. Phys.* **2005**, *77*, 1083.
[2] G. Catalan, J. Seidel, R. Ramesh, J. F. Scott, *Rev. Mod. Phys.* **2012**, *84*, 119.
[3] J. Seidel, L. W. Martin, Q. He, Q. Zhan, Y. H. Chu, A. Rother, M. E. Hawkridge, P. Maksymovych, P. Yu, M. Gajek, N. Balke, S. V. Kalinin, S. Gemming, F. Wang, G. Catalan, J. F. Scott, N. A. Spaldin, J. Orenstein, R. Ramesh, *Nat. Mater.* **2009**, *8*, 229.
[4] J. Guyonnet, I. Gaponenko, S. Gariglio, P. Paruch, *Adv. Mater.* **2011**, *23*, 5377.
[5] T. Sluka, A. K. Tagantsev, P. Bednyakov, N. Setter, *Nat. Commun.* **2013**, *4*, 1808.
[6] T. Choi, Y. Horibe, H. T. Yi, Y. J. Choi, W. Wu, S. W. Cheong, *Nat. Mater.* **2010**, *9*, 253.
[7] S. Y. Yang, J. Seidel, S. J. Byrnes, P. Shafer, C. H. Yang, M. D. Rossell, P. Yu, Y. H. Chu, J. F. Scott, J. W. Ager, L. W. Martin, R. Ramesh, *Nat. Nanotechnol.* **2010**, *5*, 143.
[8] Q. He, C. H. Yeh, J. C. Yang, G. Singh-Bhalla, C. W. Liang, P. W. Chiu, G. Catalan, L. W. Martin, Y. H. Chu, J. F. Scott, R. Ramesh, *Phys. Rev. Lett.* **2012**, *108*, 067203.
[9] T. Sluka, A. K. Tagantsev, D. Damjanovic, M. Gureev, N. Setter, *Nat. Commun.* **2012**, *3*, 748.
[10] J. F. Scott, *Science* **2007**, *315*, 954.
[11] D. Li, D. A. Bonnell, *Annu. Rev. Mater. Res.* **2008**, *38*, 351.
[12] Y. H. Chu, Q. He, C. H. Yang, P. Yu, L. W. Martin, P. Shafer, R. Ramesh, *Nano Lett.* **2009**, *9*, 1726.
[13] D. Meier, J. Seidel, A. Cano, K. Delaney, Y. Kumagai, M. Mostovoy, N. A. Spaldin, R. Ramesh, M. Fiebig, *Nat. Mater.* **2012**, *11*, 284.
[14] R. K. Vasudevan, A. N. Morozovska, E. A. Eliseev, J. Britson, J. C. Yang, Y. H. Chu, P. Maksymovych, L. Q. Chen, V. Nagarajan, S. V. Kalinin, *Nano Lett.* **2012**, *12*, 5524.
[15] B. M. Vul, G. M. Guro, I. I. Ivanchik, *Ferroelectrics* **1973**, *6*, 29.
[16] M. Schröder, A. Haußmann, A. Thiessen, E. Soergel, T. Woike, L. M. Eng, *Adv. Funct. Mater.* **2012**, *22*, 3936.
[17] W. Wu, Y. Horibe, N. Lee, S. W. Cheong, J. R. Guest, *Phys. Rev. Lett.* **2012**, *108*, 077203.
[18] Y. L. Tang, Y. L. Zhu, Y. J. Wang, W. Y. Wang, Y. B. Xu, W. J. Ren, Z. D. Zhang, X. L. Ma, *Sci. Rep.* **2014**, *4*, 4115.
[19] C. L. Jia, S. B. Mi, K. Urban, I. Vrejoiu, M. Alexe, D. Hesse, *Nat. Mater.* **2008**, *7*, 57.
[20] T. Matsumoto, R. Ishikawa, T. Tohei, H. Kimura, Q. Yao, H. Zhao, X. Wang, D. Chen, Z. Cheng, N. Shibata, Y. Ikuhara, *Nano Lett.* **2013**, *13*, 4594.
[21] W. M. Lee, J. H. Sung, K. Chu, X. Moya, D. Lee, C. J. Kim, N. D. Mathur, S. W. Cheong, C. H. Yang, M. H. Jo, *Adv. Mater.* **2012**, *24*, OP49.
[22] L. Li, P. Gao, C. T. Nelson, J. R. Jokisaari, Y. Zhang, S. J. Kim, A. Melville, C. Adamo, D. G. Schlom, X. Pan, *Nano Lett.* **2013**, *13*, 5218.
[23] C. T. Nelson, B. Winchester, Y. Zhang, S. J. Kim, A. Melville, C. Adamo, C. M. Folkman, S.-H. Baek, C. B. Eom, D. G. Schlom, L. Q. Chen, X. Pan, *Nano Lett.* **2011**, *11*, 828.
[24] A. Lubk, M. D. Rossell, J. Seidel, Q. He, S. Y. Yang, Y. H. Chu, R. Ramesh, M. J. Hÿtch, E. Snoeck, *Phys. Rev. Lett.* **2012**, *109*, 047601.
[25] Y. Wang, C. Nelson, A. Melville, B. Winchester, S. Shang, Z. K. Liu, D. G. Schlom, X. Pan, L. Q. Chen, *Phys. Rev. Lett.* **2013**, *110*, 267601.
[26] F. Zavaliche, S. Y. Yang, T. Zhao, Y. H. Chu, M. P. Cruz, C. B. Eom, R. Ramesh, *Phase Transitions* **2006**, *79*, 991.
[27] Y. Qi, Z. Chen, C. Huang, L. Wang, X. Han, J. Wang, P. Yang, T. Sritharan, L. Chen, *J. Appl. Phys.* **2012**, *111*, 104117.
[28] F. Kubel, H. Schmid, *Acta Cryst.* **1990**, *B46*, 698.
[29] C. L. Jia, K. W. Urban, M. Alexe, D. Hesse, I. Vrejoiu, *Science* **2011**, *331*, 1420.
[30] C. L. Jia, S. B. Mi, K. Urban, I. Vrejoiu, M. Alexe, D. Hesse, *Phys. Rev. Lett.* **2009**, *102*, 117601.
[31] C. L. Jia, V. Nagarajan, J. Q. He, L. Houben, T. Zhao, R. Ramesh, K. Urban, R. Waser, *Nat. Mater.* **2007**, *6*, 64.
[32] P. Gao, J. Britson, C. T. Nelson, J. R. Jokisaari, C. Duan, M. Trassin, S. H. Baek, H. Guo, L. Li, Y. Wang, Y. H. Chu, A. M. Minor, C. B. Eom, R. Ramesh, L. Q. Chen, X. Pan, *Nat. Commun.* **2014**, *5*, 3801.
[33] S. K. Streiffer, C. B. Parker, A. E. Romanov, M. J. Lefevre, L. Zhao, J. S. Speck, W. Pompe, C. M. Foster, G. R. Bai, *J. Appl. Phys.* **1998**, *83*, 2742.
[34] R. K. Vasudevan, W. Wu, J. R. Guest, A. P. Baddorf, A. N. Morozovska, E. A. Eliseev, N. Balke, V. Nagarajan, P. Maksymovych, S. V. Kalinin, *Adv. Funct. Mater.* **2013**, *23*, 2592.
[35] A. N. Morozovska, *Ferroelectrics* **2012**, *438*, 3.
[36] Y. Gu, M. Li, A. N. Morozovska, Y. Wang, E. A. Eliseev, V. Gopalan, L. Q. Chen, *Phys. Rev. B* **2014**, *89*, 174111.
[37] S. M. Anthony, S. Granick, *Langmuir* **2009**, *25*, 8152.

© 2015 WILEY-VCH Verlag GmbH & Co. KGaA, Weinheim